# UC Irvine
## UC Irvine Previously Published Works

**Title**

Three-dimensional attosecond resonant stimulated X-ray Raman spectroscopy of electronic excitations in core-ionized glycine

**Permalink**

https://escholarship.org/uc/item/5039f40n

**Journal**

Physical Chemistry Chemical Physics, 16(44)

**ISSN**

0956-5000

**Authors**

Zhang, Yu
Biggs, Jason D
Hua, Weijie
et al.

**Publication Date**

2014-11-28

**DOI**

10.1039/c4cp03361b

Peer reviewed

# Three-dimensional attosecond resonant stimulated X-ray Raman spectroscopy of electronic excitations in core-ionized glycine

Yu Zhang, Jason D. Biggs, Weijie Hua, Konstantin E. Dorfman and Shaul Mukamel*

We investigate computationally the valence electronic excitations of the amino acid glycine prepared by a sudden nitrogen core ionization induced by an attosecond X-ray pump pulse. The created superposition of cationic excited states is probed by two-dimensional transient X-ray absorption and by three dimensional attosecond stimulated X-ray Raman signals. The latter, generated by applying a second broadband X-ray pulse combined with a narrowband pulse tuned to the carbon K-edge, reveal the complex coupling between valence and core-excited manifolds of the cation.

## I. Introduction

Strong-field molecular ionization may impulsively trigger rich electronic and nuclear dynamics, geometry relaxation, molecular dissociation,[1] charge migration[2–6] and radiation emission,[7] occurring on different time scales. Ionization is also the first step in the high-harmonic generation of XUV and soft X-ray attosecond pulses,[8–11] and has been used as a tool for imaging molecular orbitals,[12–15] since the angular distribution of the ionization yield reflects the shape of the original molecular orbital.[16] A broadband superposition of valence excited states of the cation is prepared and monitored.[17] Attosecond techniques have been used to study multielectron ionization and nonadiabatic dynamics.[18,19] Photoionization has drawn considerable experimental and theoretical attention. X-ray ionization and fragmentation can be used for probing transient molecular structures in the course of photochemical reactions.[20] The photoionization of water, proteins and DNA is essential in the studies of photodamage of biomolecules.[21,22]

In this paper we study the molecule glycine impulsively ionized at the N K-edge and probed at the C K-edge by X-ray pulses. Glycine is the simplest one of the 21 amino acids found in eukaryotes. It can serve as a starting point for studying the photodamage of protein by X-ray.[23,24] Here to illustrate the principle we only simulate the N pump C probe signals, while the other type of pump and probe signals (*e.g.*, the O pump C probe signal) can be calculated in the same way. To ensure that the core hole created by this interaction is localized to a particular type of atom, the pulse is tuned just above the absorption edge of that atom. Valence electron ionization

*Dept. of Chemistry, University of California, 450 Rowland Hall, Irvine, California 92697, USA. E-mail: smukamel@uci.edu*

typically prepares a small number of cationic states populated by the ionizing pulse.[7] A larger number of cationic states are prepared by a sudden core ionization, which is faster than the electron correlation time. A typical response time for spectator electrons to a sudden removal of an electron is about 50 as.[4,25] To be impulsive, the sudden-ionizing pulse should therefore be shorter than this time. We should note that it is much easier to suddenly remove a core electron without disturbing other electrons than valence electrons, since typically a core electron is energetically well separated and more spatially localized than valence electrons.

An electron ejected from the core orbital leaves the molecule in a nonstationary superposition state which can be monitored by linear transient X-ray absorption spectroscopy (TXAS) or by nonlinear attosecond stimulated Raman spectroscopy (ASRS). Core excitations are selective because core transitions for different types of atoms are spectrally well removed from each other.[26] Only those valence excitations with transition density in the region near the selected atom will be active in a resonant X-ray Raman process.[27–29] In recent simulations we had demonstrated that stimulated X-ray Raman can be used to monitor excitation energy transfer in metalloporphyrin heterodimers[30] and long-range biological electron transfer in azurin,[31] with higher spatial and temporal resolution than possible by conventional optical or infrared techniques.

Nonlinear X-ray experiments have been made possible by the development of intense X-ray resources.[32,33] One-dimensional stimulated X-ray Raman spectroscopy (1D-SXRS) is the simplest time-domain X-ray Raman technique.[34] Here, an X-ray pump pulse is used to create a superposition of valence-excited states through a stimulated Raman process. After a variable time delay, a second X-ray pulse is used to probe the wavepacket created by the pump pulse, by recording the change in the probe's total

integrated transmitted intensity as a function of the interpulse delay. Fourier transform with respect to the delay time then reveals Raman peaks. Multidimensional extensions for this technique have been proposed.[35,36]

SXRS requires collection of the signal in the time domain and subsequent Fourier transformation to find the resonances. It is necessary to vary the interpulse delay by hundreds of femtoseconds in order to achieve adequate frequency resolution,[31] *e.g.* for a frequency resolution of $\Delta\omega = 0.05$ eV a sampling time of 82 fs is required. Much success has been had monitoring nuclear vibrational dynamics using femtosecond stimulated Raman spectroscopy (FSRS).[37,38] This technique uses a combination of narrow and broadband pulses to collect the Raman signal in a single shot, avoiding the need for a numerical Fourier transform. It should be emphasized that even though the time delay between the ionizing pulse and the broadband Raman probe is well defined, the resulting signal may not be viewed as an instantaneous snapshot of the Raman spectrum, and it must be averaged over the dephasing time of the final state.[39,40] Our proposed technique, ASRS, extends FSRS to the X-ray regime. For atom-selective excitation we further use resonant rather than off-resonant pulses. In an ASRS experiment, two X-ray pulses, the narrowband pump and broadband probe, which overlap in time but not frequency, arrive with a fixed delay after ionization. In an earlier study we applied this technique to photoinduced long-range electron transfer.[31] Here we study sudden ionization. The details of ASRS will be given in Section IV.

In Section II we give a brief description of our theoretical model and computational details. TXAS is presented in Section III and ASRS signals are presented and analyzed in Section IV. Finally conclusions and possible future directions are discussed in Section V.

## II. Theoretical and computational methods

Within the sudden ionization approximation,[41] other electrons have no time to react to the impulsively created hole, so that the prepared nonstationary cationic state can be described by simply removing one electron from a single molecular orbital while the other electrons remain in their original self-consistent molecular orbitals of the ground state.[2,7,42] The nonstationary state can be expanded in eigenstates of the cation as

$$|\Psi_{ns}\rangle = \sum_a C_a |a\rangle. \tag{1}$$

Here, $C_a = \langle a|\Psi_{ns}\rangle$.

Our targeted molecule glycine serves as a model for studying amino acid ionization. One N 1s core electron is removed and after some time delay the ionized molecule is probed at the C K-edge. The ground-state geometry was optimized using the quantum chemistry package Gaussian09[43] at the B3LYP[44,45]/6-311G** level. The nonstationary cationic state was obtained

by removing a single N 1s electron from the self-consistent Kohn–Sham configuration of the neutral molecule. The lowest N1s-ionized eigenstate $|a_0\rangle$ was obtained by a self-consistent Kohn–Sham calculation which keeps the N 1s hole, and higher eigenstates were approximately generated by permuting the occupied and virtual orbitals of $|a_0\rangle$.[34] Core excitations were calculated using restricted excitation window time-dependent density functional theory(REW-TDDFT).[46–50] The cc-pVTZ[51] basis set was used for C and N, and the basis set 6-311G** was used for other elements. REW-TDDFT and transition dipole calculations were performed with a locally modified version of NWChem code[52] with the B3LYP functional and the Tamm–Dancoff approximation.[53] The transition dipole calculation protocol was given in ref. 50 and 54.

## III. Transient absorption of a resonant X-ray probe

Interaction with the nitrogen core-ionizing pulse $\mathbf{k}_1$ at time $t = 0$ leaves the molecule in the superposition state eqn (1). Truncating the coefficients at $|C_a| > 0.04$ leaves us with 27 cationic states. Fig. 1 shows the distribution of the expansion coefficients in eqn (1).

We first consider the transient absorption of an X-ray pulse resonant with the carbon K-edge. At time $t = \tau$, an attosecond probe pulse arrives and its frequency-dispersed spectrum is recorded. The signal is defined as the change in the probe absorption caused by the pump pulse, and recorded as a function of the delay time $\tau$ and the spectrometer frequency $\omega$.

The transient absorption (TA) signal can be read off the loop diagram shown in Fig. 2 in the frequency domain using the rotating wave approximation and treating pulse $\varepsilon_1$ explicitly as

$$S_{TA}(\tau,\omega) = -\Im \sum_{a \neq b,x} \int \frac{d\omega_1}{2\pi} \frac{d\omega_1'}{2\pi} \frac{d\omega_2}{2\pi} \varepsilon_2^*(\omega)\varepsilon_2(\omega_2)\varepsilon_1^*(\omega_1)\varepsilon_1(\omega_1')$$
$$\times e^{-i(\omega-\omega_2)\tau} 2\pi\delta(\omega - \omega_2 + \omega_1 - \omega_1')$$
$$\times V_{gb}V_{bx}V_{xa}^*V_{ag}^* G_b^\dagger(\omega_1)G_x(\omega_1' + \omega_2)G_a(\omega_1'). \tag{2}$$

Here a and b are valence states (including the cationic ground state), x is a core-excited state, $V_{ij}$ is the transition dipole moment between states i and j, $\varepsilon_j(\omega)$ is the spectral
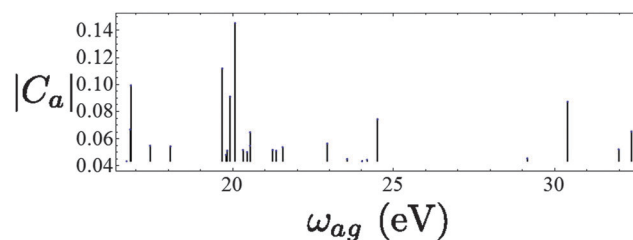


**Fig. 1** Modulus of the expansion coefficients *versus* excitation energy for the impulsively ionized Glycine molecule. The ground-state contribution is omitted.
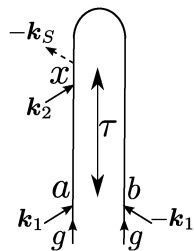
**Fig. 2** Loop diagram for the time-resolved X-ray absorption experiment. $\mathbf{k}_1$ is the actinic pulse. $\mathbf{k}_2$ is the probe pulse and $\mathbf{k}_s$ is the signal. g is the ground-state of the neutral molecule, a and b are valence-states of the cation with a nitrogen 1s core hole, and x is a two-core-hole state.

envelope of the jth pulse, and $G(\omega) = 1/\hbar[\omega - H/\hbar + i\epsilon]$ is the frequency domain retarded Green's function. We have removed the a = b term, which provides a DC ($\tau$-independent) background. We take $\varepsilon_1(t) = \varepsilon_1 \delta(t)$ (sudden approximation), allowing us to carry out the integrals in eqn (2) to obtain

$$S_{TA}(\tau, \omega) = -\Im \frac{1}{\hbar^3} V_{bx} V_{xa}^* \theta(\tau) \frac{\varepsilon_2^*(\omega)\varepsilon_2(\omega + \omega_{ba})\rho_{ab}(\tau)}{\omega - \omega_{xb} + i\gamma_{xb}}, \quad (3)$$

where $\omega_{\alpha\beta} = \omega_\alpha - \omega_\beta$, $\gamma_{\alpha\beta} = \gamma_\alpha + \gamma_\beta$, and

$$\rho_{ab}(t) = |\varepsilon_1|^2 C_b^* C_a e^{-i\omega_{ab}t - \gamma_{ab}t}, \quad (4)$$

is the initially prepared ionic state as described in Section II.

These calculations neglect nuclear motion. The initial ionic state in this experiment has a nitrogen core hole, and therefore has a very short lifetime due to Auger decay (7.3 fs corresponding to the linewidth in eqn (3)).[26] This implies that the entire signal is collected on a very fast timescale in comparison to nuclear motion, and the assumption is justified.

In Fig. 3 we show the carbon K-edge TXAS signal following ionization of the nitrogen 1s core electron, with the a = b term from eqn (3) included (top panel) and removed (bottom panel) We assume a 50 as pulse centered at 270 eV, whose power spectrum is also shown. We take the lifetime broadening of the ionic state with a nitrogen core-hole to be $\gamma_a = 0.09$ eV and estimate that of the double-core hole state to be $\gamma_x = 0.2$ eV. The total signal, top panel, is dominated by the absorption from
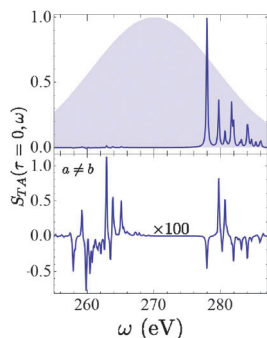


**Fig. 3** The carbon K-edge TXAS signal $S_{TA}(\tau, \omega)$ from glycine following N K-edge ionization, with the interpulse delay set to zero, given by eqn (3), with the a = b DC term included top panel but omitted from the bottom panel. The shaded region in the upper panel shows the power spectrum of the probe pulse $|\varepsilon_2(\omega)|^2$.
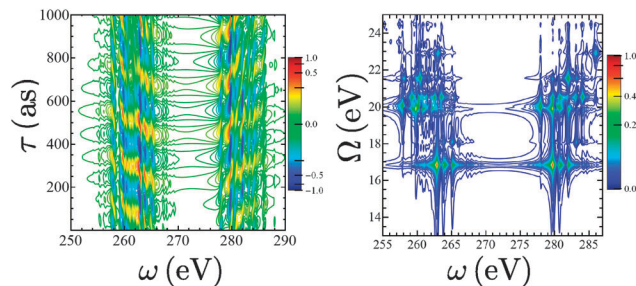


**Fig. 4** Left: time-domain TXAS signal $S_{TA}(\tau, \omega)$, given by eqn (3). Right: modulus of the frequency-domain TXAS spectrum $|S_{TA}(\Omega, \omega)|$, given by eqn (5). 2D signals are plotted using a nonlinear scale, shown in the colorbars, which interpolates between linear for small features and logarithmic for larger peaks. See ref. 55 for details regarding the plotting scale.

the ground state population. Removal of this background reveals the coherence-dependent signal, in the bottom panel, which shows both absorption from the ground cationic state, with energies $> 277$ eV, and from valence-excited states, between 255 eV and 270 eV.

The signal is collected *versus* the interpulse delay $\tau$. The left panel of Fig. 4 shows $S_{TA}(\tau, \omega)$ for interpulse delays up to 1 fs, with the DC background removed. The signal shows strong oscillations with period between 200 as and 250 as. Fourier transformation with respect to the delay time reveals the correlation between the initial coherence $\rho_{ab}$ and the core-excited state. Taking the Fourier transform of eqn (3) with respect to $\tau$ results in

$$\begin{aligned}
S_{TA}(\Omega, \omega) &= \int_{-\infty}^{\infty} d\tau S_{TA}(\tau, \omega) e^{i\Omega T} \\
&= \frac{1}{2\hbar^3} \left( \frac{V_{bx}^* V_{xa} \varepsilon_2(\omega) \varepsilon_2^*(\omega + \omega_{ba}) C_a C_b^*}{[\omega - \omega_{xb} - i\gamma_{xb}][\Omega + \omega_{ab} + i\gamma_{ab}]} \right. \\
&\quad \left. - \frac{V_{bx} V_{xa}^* \varepsilon_2^*(\omega) \varepsilon_2(\omega + \omega_{ba}) C_a^* C_b}{[\omega - \omega_{xb} + i\gamma_{xb}][\Omega - \omega_{ab} + i\gamma_{ab}]} \right).
\end{aligned} \quad (5)$$

Experimentally, the signal must be collected for a finite sampling time and transformed numerically, which will introduce a width to the peaks. However, lifetime broadening dominates the finite time sampling effects, see Appendix A for more details.

Each term in eqn (5) is a product of two factors. The first reveals valence frequencies $\omega_{ab}$ and the density matrix $C_a^* C_b$ prepared by the ionization process. This is our relevant spectroscopic information. The second factor is an observation window that depends on the carbon core transition $\omega_{xb}$.

The right panel of Fig. 4 shows the modulus Fourier transform signal $|S_{TA}(\Omega, \omega)|$, eqn (5). The dispersed frequency $\omega$ gives the energy difference $\omega_{xb}$ between the double core-hole state x and the cationic valence state b, while the Fourier transform frequency $\Omega$ gives the energy difference $\omega_{ab}$ between valence states of the cation with a single core hole. We focus on the portion where $\Omega > 16$ eV, corresponding to the case where either state a or b are in the cation ground state, and the other is a valence excitation. The $\omega$ peaks are centered around $\omega = 260$ eV (absorption by the valence excited state) and $\omega = 280$ eV (absorption by the ground state).

# IV. Attosecond stimulated X-ray raman spectroscopy

## A. The signal

ASRS uses two probe pulses; $\mathbf{k}_2$ is narrowband (tens of femto-seconds) and on resonance with a core transition, and $\mathbf{k}_3$ is broadband (tens to hundreds of attoseconds), and redshifted from the first as shown in Fig. 5. The frequency-dispersed transmission of the broadband pulse is a 3D signal given by the two diagrams in Fig. 5

$$S_{\text{ASRS}} = S_{\text{i}} + S_{\text{ii}} \tag{6}$$

where $S_{\text{i}}$ and $S_{\text{ii}}$ are read off the loop diagrams as

$$
\begin{aligned}
&S_{\text{i}}(\omega - \omega_2, \tau, \omega_2) \\
&= \Im \int \frac{d\omega_1}{2\pi} \frac{d\omega_1'}{2\pi} \frac{d\omega_3}{2\pi} \varepsilon_s{}^*(\omega) \varepsilon_3(\omega_3) |\varepsilon_2|^2 \varepsilon_1{}^*(\omega_1) \varepsilon_1\left(\omega_1'\right) \\
&\quad \times e^{i\left(\omega_1 - \omega_1'\right)\tau} \sum_{abcxy} V_{gb} V_{bx} V_{xc}{}^* V_{cy} V_{ya}{}^* V_{ag}{}^* \\
&\quad \times 2\pi\delta\left(\omega - \omega_3 + \omega_1 - \omega_1'\right) G_b^\dagger(\omega_1) G_x^\dagger(\omega_1 + \omega_2) \\
&\quad \times G_c^\dagger(\omega_1 + \omega_2 - \omega_3) G_y\left(\omega_2 + \omega_1'\right) G_a\left(\omega_1'\right),
\end{aligned}
\tag{7}
$$

and

$$
\begin{aligned}
&S_{\text{ii}}(\omega - \omega_2, \tau, \omega_2) \\
&= \Im \int \frac{d\omega_1}{2\pi} \frac{d\omega_1'}{2\pi} \frac{d\omega_3}{2\pi} \varepsilon_s{}^*(\omega) \varepsilon_3(\omega_3) |\varepsilon_2|^2 \varepsilon_1{}^*(\omega_1) \varepsilon_1\left(\omega_1'\right) \\
&\quad \times e^{i\left(\omega_1 - \omega_1'\right)\tau} \sum_{abcxy} V_{gb} V_{bx} V_{xc}{}^* V_{cy} V_{ya}{}^* V_{ag}{}^* \\
&\quad \times 2\pi\delta\left(\omega - \omega_3 + \omega_1 - \omega_1'\right) G_b^\dagger(\omega_1) G_x\left(\omega_1' + \omega_3\right) \\
&\quad \times G_c\left(\omega_1' + \omega_3 - \omega_2\right) G_y\left(\omega_1' + \omega_3\right) G_a\left(\omega_1'\right).
\end{aligned}
\tag{8}
$$

Here we have assumed a monochromatic pump pulse $\varepsilon_2(t) = \varepsilon_2 e^{-i\omega_2(t-\tau)}$. A 30 fs Raman pump has a FWHM bandwidth 0.06 eV, which is narrower than the lifetime broadening of the core hole state (0.1 eV),[26] and the assumption is justified under these conditions. Evaluating the integrals in eqn (7) and (8), again assuming an impulsive ionizing pump, we obtain

broadband pulse followed by emission into the narrowband frequency. Traditionally, the FSRS experiment is performed far off resonance, where $S_{\text{i}}$ and $S_{\text{ii}}$ will give Stokes and anti-Stokes peaks, respectively. Note that since $S_{\text{i}}$ depends on $\omega - (\omega_2 - \omega_{\text{ca}})$ and $S_{\text{ii}}$ depends on $\omega - (\omega_2 + \omega_{\text{cb}})$, the Stokes and anti-Stokes peaks will show up at the same Raman shift with opposite sign, acting to cancel each other. In the absence of the actinic pump, the system is in the ground state initially, and $S_{\text{ii}}$ vanishes. More complicated lineshapes can arise when the narrowband frequency is on resonance with a given ground-state to core-excited state transition, or when the broadband probe covers the core excitation spectrum from valence-excited states.

## B. 1D ASRS results

In Fig. 6 we show the ASRS signal with $S_{\text{ASRS}}(\omega - \omega_2, \tau = 0 \text{ as}, \omega_2 = 277 \text{ eV})$, taking the broadband pulse to have center frequency $\omega_3 = 260 \text{ eV} = \omega_2 - 17 \text{ eV}$, and a FWHM bandwidth of 11 eV. The signal is plotted *versus* the Raman shift $\omega - \omega_2$, to reveal the valence-excitation energies. $S_{\text{i}}$ shows a large elastic (Rayleigh) peak with the Raman shift $\omega - \omega_2 = 0$, and a cluster of peaks with shifts between $-24$ eV and $-16$ eV which correspond to Stokes transitions where the final state is of higher energy than the initial, *i.e.* where $\omega_{\text{ca}} > 0$.

$S_{\text{ii}}$ is more complex since the detected frequency $\omega$ shows up in all three of the terms in the denominator of eqn (10). This means that a single term in the summation of eqn (10) may contribute three different peaks, corresponding to $\omega = \omega_{\text{xb}}$, $\omega = \omega_{\text{yb}}$, and $\omega = \omega_2 + \omega_{\text{cb}}$. The first two Green's functions in eqn (10) give peaks correspond to absorption from excited valence states, and the peak positions must be interpreted in terms of the actual monochromator frequency $\omega$, rather than the Raman shift $\omega - \omega_2$. These we refer to as absorption peaks. The third Green's function in eqn (10) gives a Raman-type peak, since it is the shifted frequency that reveals a system resonance.

The $S_{\text{ii}}$ signal shown in the middle panel of Fig. 6 contains a Rayleigh peak, with opposite sign to the peak in $S_{\text{i}}$, and a dispersive peak at a shift of $\omega - \omega_2 = 1$ eV corresponding to absorption of the Raman probe, *i.e.* to the term in the summation of eqn (10) where the states a and b are the cationic ground state and x and y are the lowest-energy two-core-hole state. Weaker peaks with Raman shifts between $-20$ eV and $-11$ eV contain both anti-Stokes transitions, where the final state is lower in energy and $\omega_{\text{cb}} < 0$, and

$$
S_{\text{i}}(\omega - \omega_2, \tau, \omega_2) = -\Im \sum_{a \neq b, cxy} \frac{1}{\hbar^5} \frac{V_{bx} V_{xc}{}^* V_{cy} V_{ya}{}^* \varepsilon_s{}^*(\omega) \varepsilon_3(\omega - \omega_{ab}) |\varepsilon_2|^2 \rho_{ab}(\tau)}{\left[\omega_2 - \omega_{xb} - i(\gamma_x - \gamma_b)\right]\left[\omega_2 - \omega_{ya} + i\left(\gamma_y - \gamma_a\right)\right]\left[\omega - (\omega_2 - \omega_{ca}) + i\gamma_{ac}\right]},
\tag{9}
$$

and

$$
S_{\text{ii}}(\omega - \omega_2, \tau, \omega_2) = \Im \sum_{a \neq b, cxy} \frac{1}{\hbar^5} \frac{V_{bx} V_{xc}{}^* V_{cy} V_{ya}{}^* \varepsilon_s{}^*(\omega) \varepsilon_3(\omega - \omega_{ab}) |\varepsilon_2|^2 \rho_{ab}(\tau)}{\left[\omega - \omega_{xb} + i\gamma_{xb}\right]\left[\omega - \omega_{yb} + i\gamma_{yb}\right]\left[\omega - (\omega_2 + \omega_{cb}) + i\gamma_{cb}\right]}.
\tag{10}
$$

$S_{\text{i}}$ and $S_{\text{ii}}$ represent different processes. $S_{\text{i}}$, in which $\omega_2$ excites and the broadband probe stimulates emission, represents the time-domain analogue of resonant inelastic X-ray scattering (RIXS) technique. $S_{\text{ii}}$ involves the absorption of the

absorption of the probe by higher valence excited states. Under these conditions, the anti-Stokes transitions occur in the same part of the spectrum as absorption from valence-excited states to the low-lying two-core-hole states, and the processes may not be well separated.
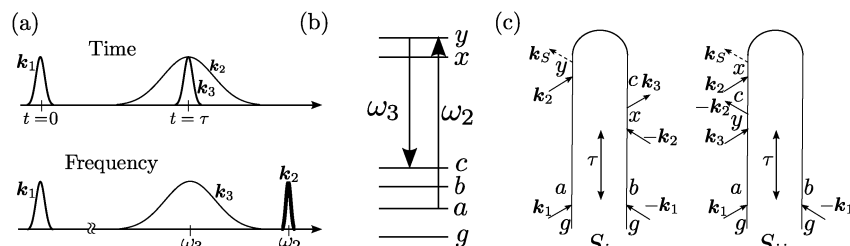
**Fig. 5** (a) Pulse sequence for the narrow pump/broad probe stimulated Raman experiment. (b) Level scheme. (c) The two contributing loop diagrams. g is the ground-state of the neutral molecule, a, b and c are valence-states of the cation with a nitrogen 1s core hole, and x and y are two-core-hole states.
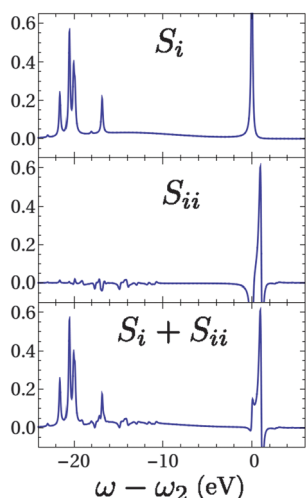


**Fig. 6** The ASRS signal at the carbon K-edge $S_{ASRS}(\omega - \omega_2, \tau = 0, \omega_2 = 277$ eV), eqn (6)–(10). Shown are $S_i$, $S_{ii}$, and their sum, as indicated.



**Fig. 7** Time-dependent ASRS signal $S_{ASRS}(\omega - \omega_2, \tau, \omega_2 = 277$ eV).

### C.  2D ASRS signals

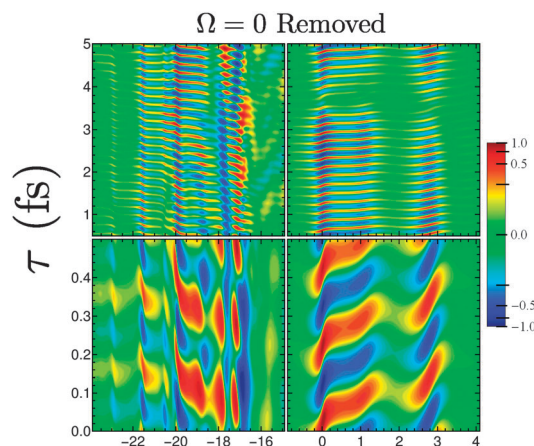Fig. 7 shows the $\tau$-dependent ASRS signal for interpulse delays up to 5 fs. The peaks with a positive Raman shift, which arise exclusively from $S_{ii}$ absorption-type resonances, show strong features between $\omega - \omega_2 = 0$–3 eV at early times, even at zero interpulse delay. The Raman peaks, with $\omega - \omega_2$ between $-17$ eV and $-22$ eV, start weak and get stronger, with a maximum around $\tau = 122$ as. Since the ASRS signal is taken

at the carbon K-edge, this could reveal the timescale for the valence relaxation, due to the sudden appearance of the nitrogen core-hole, to propagate to the carbon atoms.

In $S_{ASRS}(\omega - \omega_2, \Omega, \omega_2)$, given by

$$
\begin{aligned}
S(\omega - \omega_2, \Omega, \omega_2) &= \int_{-\infty}^{\infty} d\tau S(\omega - \omega_2, \tau, \omega_2) e^{i\Omega\tau} = \frac{1}{2\hbar^5} \sum_{abcxy} \frac{C_a C_b^* V_{cy} V_{ya}^\dagger V_{bx} V_{xc}^\dagger |\varepsilon_2|^2 \varepsilon^*(\omega) \varepsilon_3(\omega - \omega_{ab})}{\Omega - \omega_{ab} + i\gamma_{ab}} \\
&\times \left( \frac{-1}{[\omega_2 - \omega_{xb} - i(\gamma_x - \gamma_b)][\omega_2 - \omega_{ya} + i(\gamma_y - \gamma_a)][\omega - \omega_2 - \omega_{ac} + i\gamma_{ac}]} \right. \\
&\left. + \frac{1}{[\omega - \omega_{xb} + i\gamma_{xb}][\omega - \omega_{yb} + i\gamma_{yb}][\omega - \omega_2 - \omega_{cb} + i\gamma_{cb}]} \right) + \frac{\left(C_a C_b^* V_{cy} V_{ya}^\dagger V_{bx} V_{xc}^\dagger |\varepsilon_2|^2 \varepsilon^*(\omega) \varepsilon_3(\omega - \omega_{ab})\right)^*}{\Omega + \omega_{ab} + i\Gamma_{ab}} \\
&\times \left( \frac{-1}{[\omega_2 - \omega_{xb} + i(\gamma_x - \gamma_b)][\omega_2 - \omega_{ya} - i(\gamma_y - \gamma_a)][\omega - \omega_2 - \omega_{ac} - i\gamma_{ac}]} \right. \\
&\left. + \frac{1}{[\omega - \omega_{xb} + i\gamma_{xb}][\omega - \omega_{yb} + i\gamma_{yb}][\omega - \omega_2 - \omega_{cb} + i\gamma_{cb}]} \right)
\end{aligned}
\tag{11}
$$

we can separate the contributions from coherences and populations, which show up at $\Omega = 0$ eV and $\Omega > 0$ eV, respectively. The $\Omega = 0$ contribution, shown in Fig. 8A and B, is largely the same as the $\tau = 0$ signal described above. Stokes Raman transitions, originating from $S_i$, from the ground state population
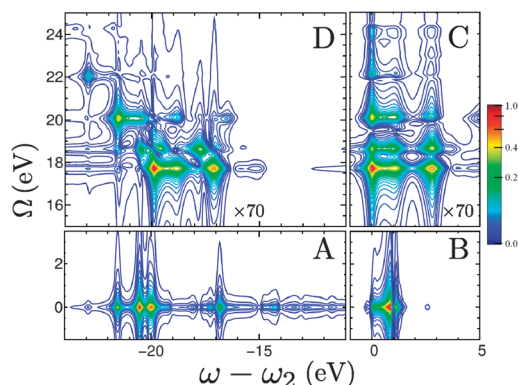
**Fig. 8** Modulus Fourier transform ASRS signal, $|S_{\text{ASRS}}(\omega - \omega_2, \Omega, \omega_2 = 277 \text{ eV})|$, given by eqn (11), split into four different regions. Regions A and B show the signal from initial populations, while regions C and D show the signal from coherences.
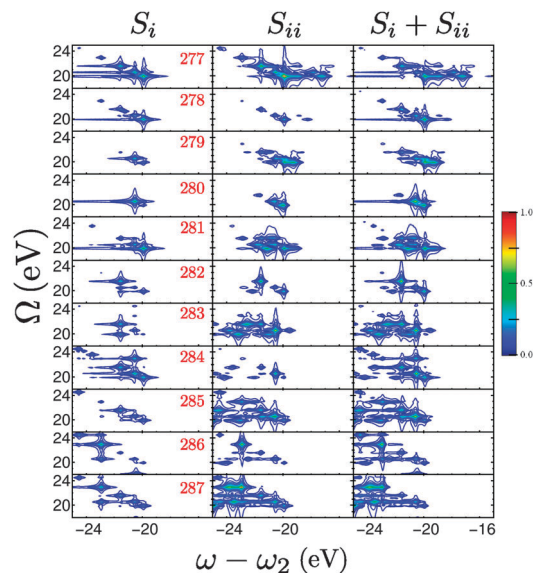


**Fig. 10** 2D slices of the 3D signal $|S_{\text{ASRS}}(\Omega, \omega; \omega_2)|$ plotted in Fig. 9 for different values of the narrowband frequency $\omega_2$, which is indicated in red for each row.

can be found in panel A, with Raman shifts above 17 eV. However, there are also $\Omega = 0$ peaks (still in panel A) with Raman shifts between 10 eV and 15 eV, but there are no valence-excited states with these energies. Therefore these peaks represent absorption from high-lying valence-excited states into low-lying states in the two-core-hole manifold originating from diagram $S_{\text{ii}}$, rather than Raman transitions. Panel B shows absorption by the ground state population. Panels C and D show signals originating from coherences, and have been multiplied by 70 prior to plotting. Panel C gives absorption peaks, since the Raman shift is much smaller than any valence excitation energy. Panel D is the most interesting portion of the signal. It features Stokes and anti-Stokes Raman transitions, from diagrams $S_{\text{i}}$ and $S_{\text{ii}}$, respectively, as well as absorption peaks from diagram $S_{\text{ii}}$.

### D. 3D ASRS signals

In Fig. 9 we plot the 3D signal $S_{\text{ASRS}}(\omega - \omega_2, \Omega, \omega_2)$, obtained by varying the narrowband frequency $\omega_2$ between 277 eV and 287 eV. The broadband pulse center frequency is kept constant with respect to the narrowband frequency, $\omega_3 = \omega_2 - 17$ eV. We plot the $S_{\text{i}}$ and $S_{\text{ii}}$ contributions separately, and also the total signal.

We see a considerable change in the signal as $\omega_2$ is tuned into resonance with different two-core states. $S_{\text{i}}$ has its strongest peak at $(\omega - \omega_2, \Omega, \omega_2) = (-19.98 \text{ eV}, 20.54 \text{ eV}, 279.8 \text{ eV})$. This is due to the fact that both the ground state and the 10th valence-excited state (whose energy is equal to 20.54 eV) both have a core-excited state with transition frequency of 279.8 eV. $S_{\text{ii}}$ has its strongest peak at $(\omega - \omega_2, \Omega, \omega_2) = (-19.42 \text{ eV}, 19.91 \text{ eV}, 279.7 \text{ eV})$, which is mainly due to the fact that the 9th valence-excited state (whose energy is equal to 19.91 eV) has a strong core-absorption at 260.3 eV. The strong features in $S_{\text{i}}$ are due to Raman scattering while those in $S_{\text{ii}}$ are due to absorption of the probe.

2D slices of the 3D data of Fig. 9 are shown in Fig. 10, for constant values of $\omega_2$, split up into contributions from $S_{\text{i}}$ and $S_{\text{ii}}$. For all values of $\omega_2$ the $S_{\text{ii}}$ contribution is much larger than $S_{\text{i}}$, unlike the time domain $\tau = 0$ signal from eqn (5) which is dominated by the $\Omega = 0$ DC component. $S_{\text{i}}$ has a vertical peak pattern,
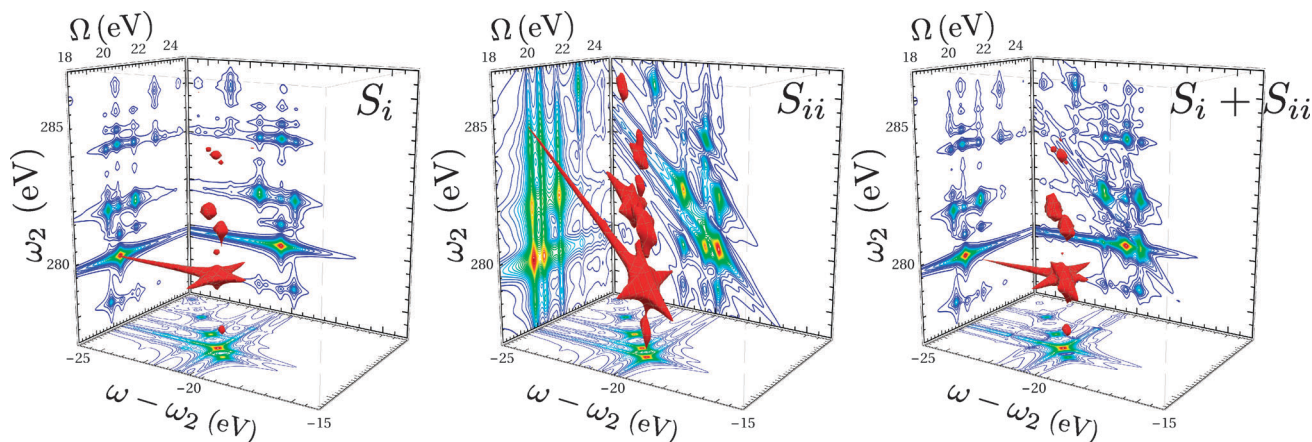


**Fig. 9** Three-dimensional plot for the modulus Fourier transform of the ASRS signal, $|S(\omega - \omega_2, \Omega, \omega_2)|$. Also shown with the 3D contour plot are 2D projections, defined as the integral of the modulus signal over the plotted region.
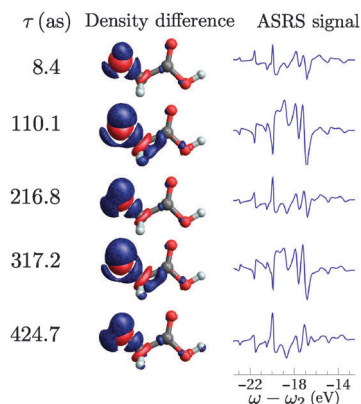
**Fig. 11** Density difference for the state following ionization, defined as the ground-state density minus the time-dependent density for the cationic wavepacket, for different time delays alongside the corresponding dynamic Raman signals (shown in Fig. 7). Red isosurfaces show negative differences, and blue surfaces show positive difference.

occurring at a constant Raman shift, and a diagonal pattern in $S_{ii}$. This is due to the $(\omega + \omega_{ca} - \omega_2 + i\gamma_{ca})^{-1}$ term in eqn (9). Differences in $S_i$ with changing $\omega_2$ are due to the fact that each core-excited states can be coupled to different valence states. $S_{ii}$ contains both Raman and absorption features, as described in Section B, coming from the $(\omega - (\omega_2 - \omega_{cb}))^{-1}$ and $(\omega - \omega_{yb} + i\Gamma_y)^{-1}(\omega - \omega_{xb} + i\Gamma_x)^{-1}$ terms in eqn (10), respectively. The absorption resonances depend only on $\omega$, and so give diagonal features when plotted as a function of Raman shift.

#### E. ASRS signal *vs.* charge density changes

In Fig. 11 we show the electronic density difference, defined as the time-dependent density of the cation minus the ground state electronic density, for five different times which correspond with the maxima and minima for the Raman peak at $\omega - \omega_2 = -17.2$ eV. The large number of states with nonnegligible amplitude in the expansion of eqn (1), shown in Fig. 1, indicates a collective motion. A negative difference-density in the region surrounding the nitrogen atom represents the removed electron. Positive electron density difference corresponds to relaxation of the system in the presence of the hole. The fact that this relaxation is already present to some extent at short time delays is attributable to the truncation of the eigenstate basis used to

project the initial state. A truncated basis must be used since the Raman signal, eqn (6)–(10), scales as the number of valence-states cubed. The lower panels of Fig. 11 show considerable changes in the electronic density in the region around the two carbon atoms at $\tau = 110.1$ as and 317.2 as. For interpulse delays of 216.8 as and 424.7 the density changes around the carbon atoms is diminished. This matches the oscillation pattern seen in the time-dependent Raman peaks in the right column of Fig. 11, showing that time-dependent ASRS is a powerful method for observing ultrafast electronic wavepacket motion following ionization. Movie S1 shows the changing density difference alongside the coherence ASRS signal for delays up to 10 fs.

## V. Conclusions

We have investigated the electronically excited states of the amino acid glycine following sudden ionization of an inner-shell nitrogen 1s electron. The signal is obtained by Raman scattering of an attosecond X-ray pulse tuned to the carbon K-edge. Transient absorption can be used to observe the changes in the core excited states, while stimulated X-ray Raman reveals valence electronic excitations. Correspondence between the time-dependent ASRS signal and changes in the electronic density are seen for short times following ionization. However, the ASRS signal depends upon the multielectron dynamics, while the density is a single electron property and not as sensitive to interference effects, so correspondence at later times is not as obvious.

Resonant X-ray Raman spectroscopy signals show the evolution of the valence excited state wavepacket created by the sudden ionization. The three-dimensional ASRS technique can be used to study more complicated electron dynamics.[20]

## Appendix A: signals with finite time sampling

The TXAS and ASRS signals are collected as a function of the interpulse delay $\tau$ and Fourier transformed to reveal the resonances involved during that time period. Experimentally, this transformation must be performed numerically using a finite time period. Mathematically, this corresponds to multiplying
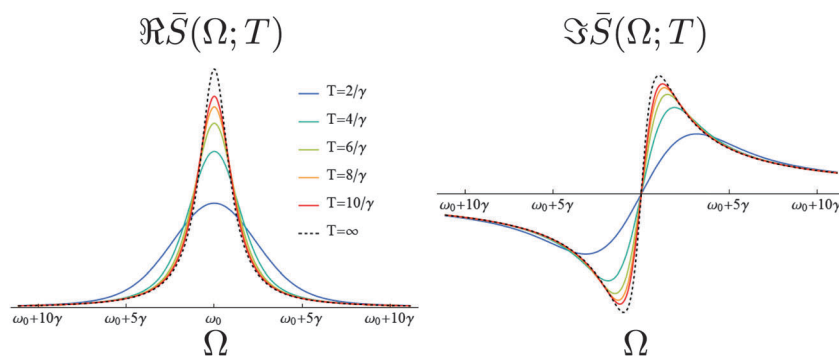


**Fig. 12** Eqn (A.5) for various values of $T$.

the continuous signal by a window function prior to the application of the Fourier transform

$$\bar{S}(\Omega; T) = \int_{-\infty}^{\infty} d\tau S(\tau) W(\tau; T) e^{i\Omega\tau}, \qquad (A.1)$$

By the convolution theorem, this can be written

$$\bar{S}(\Omega) = \int_{-\infty}^{\infty} d\omega' S(\Omega) W(\Omega - \omega'). \qquad (A.2)$$

The simplest window to use is a rectangular function whose Fourier transform is a Sinc function, which introduces significant sidelobe artifacts to the signal. This can be alleviated by using a Gaussian window function,[56] defined by

$$W_{\mathrm{G}}(t; T) = e^{-\frac{1}{2}\left(\frac{t}{T/4}\right)^2}. \qquad (A.3)$$

The signals described here are written as a sum of damped oscillations, with complex amplitudes. As an example, we look at the following signal, with a single term,

$$S(t) = \theta(t) A e^{-i\omega_0 t - \gamma t}. \qquad (A.4)$$

Plugging eqn (A.4) and (A.3) into eqn (A.1), we get

$$\bar{S}(\Omega; T) = \sqrt{\pi/2} \frac{T}{4} w\left(\frac{T}{4\sqrt{2}}(\Omega - \omega_0 + i\gamma)\right), \qquad (A.5)$$

where

$$w(z) = e^{-z^2} \mathrm{erfc}(-iz) = e^{-z^2}\left(1 + \frac{2i}{\sqrt{\pi}}\int_0^z dt e^{-t^2}\right)$$

is the Faddeeva function,[57] which is related to the Voigt profile.[58] In Fig. 12 we show the effects of a Gaussian windowing function on a single peak.

## Acknowledgements

## References

1  R. Schinke, *Photodissociation Dynamics: Spectroscopy and Fragmentation of Small Poly-atomic Molecules*, Cambridge University Press, 1995.

2  R. Weinkauf, P. Schanen, A. Metsala, E. W. Schlag, M. Bürgle and H. Kessler, *J. Phys. Chem.*, 1996, **100**, 18567.

3  L. Cederbaum and J. Zobeley, *Chem. Phys. Lett.*, 1999, **307**, 205.

4  J. Breidbach and L. S. Cederbaum, *Phys. Rev. Lett.*, 2005, **94**, 033901.

5  F. Remacle and R. D. Levine, *Proc. Natl. Acad. Sci. U. S. A.*, 2006, **103**, 6793.

6  J. Breidbach and L. S. Cederbaum, *J. Chem. Phys.*, 2007, **126**, 034101.

7  A. I. Kuleff and L. S. Cederbaum, *Phys. Rev. Lett.*, 2011, **106**, 053001.

8  J. L. Krause, K. J. Schafer and K. C. Kulander, *Phys. Rev. Lett.*, 1992, **68**, 3535.

9  P. Corkum, *Phys. Rev. Lett.*, 1993, **71**, 1994.

10  K. T. Kim, D. M. Villeneuve and P. B. Corkum, *Nat. Photonics*, 2014, **8**, 187.

11  T. J. A. Wolf, T. S. Kuhlman, O. Schalk, T. J. Martínez, K. B. Møller, A. Stolow and A.-N. Unterreiner, *Phys. Chem. Chem. Phys.*, 2014, **16**, 11770.

12  J. Itatani, J. Levesque, D. Zeidler, H. Niikura, H. Pepin, J. C. Kieffer, P. B. Corkum and D. M. Villeneuve, *Nature*, 2004, **432**, 867.

13  W. H. E. Schwarz, *Angew. Chem., Int. Ed.*, 2006, **45**, 1508.

14  S. Haessler, J. Caillat, W. Boutu, C. Giovanetti-Teixeira, T. Ruchon, T. Auguste, Z. Diveki, P. Breger, A. Maquet, B. Carre, R. Taieb and P. Salieres, *Nat. Phys.*, 2010, **6**, 200.

15  M. Kotur, T. C. Weinacht, C. Zhou and S. Matsika, *Phys. Rev. X*, 2011, **1**, 021010.

16  O. Njoya, S. Matsika and T. Weinacht, *ChemPhysChem*, 2013, **14**, 1451.

17  E. Goulielmakis, Z.-H. Loh, A. Wirth, R. Santra, N. Rohringer, V. S. Yakovlev, S. Zherebtsov, T. Pfeifer, A. M. Azzeer, M. F. Kling, S. R. Leone and F. Krausz, *Nature*, 2010, **466**, 739.

18  M. Spanner, J. Mikosch, A. Gijsbertsen, A. E. Boguslavskiy and A. Stolow, *New J. Phys.*, 2011, **13**, 093010.

19  A. E. Boguslavskiy, J. Mikosch, A. Gijsbertsen, M. Spanner, S. Patchkovskii, N. Gador, M. J. J. Vrakking and A. Stolow, *Science*, 2012, **335**, 1336.

20  V. S. Petrović, M. Siano, J. L. White, N. Berrah, C. Bostedt, J. D. Bozek, D. Broege, M. Chalfin, R. N. Coffee, J. Cryan, L. Fang, J. P. Farrell, L. J. Frasinski, J. M. Glownia, M. Guhr, M. Hoener, D. M. P. Holland, J. Kim, J. P. Marangos, T. Martinez, B. K. McFarland, R. S. Minns, S. Miyabe, S. Schorb, R. J. Sension, L. S. Spector, R. Squibb, H. Tao, J. G. Underwood and P. H. Bucksbaum, *Phys. Rev. Lett.*, 2012, **108**, 253006.

21  J. Li, Z. Nie, Y. Y. Zheng, S. Dong and Z.-H. Loh, *J. Phys. Chem. Lett.*, 2013, **4**, 3698.

22  C. Butchosa, S. Simon and A. A. Voityuk, *Org. Biomol. Chem.*, 2010, **8**, 1870.

23  J. Yano, J. Kern, K.-D. Irrgang, M. J. Latimer, U. Bergmann, P. Glatzel, Y. Pushkar, J. Biesiadka, B. Loll, K. Sauer, J. Messinger, A. Zouni and V. K. Yachandra, *Proc. Natl. Acad. Sci. U. S. A.*, 2005, **102**, 12047.

24  M. C. Corbett, M. J. Latimer, T. L. Poulos, I. F. Sevrioukova, K. O. Hodgson and B. Hedman, *Acta Crystallogr., Sect. D: Biol. Crystallogr.*, 2007, **63**, 951.

25  A. I. Kuleff and L. S. Cederbaum, *Phys. Rev. Lett.*, 2007, **98**, 083201.

26  G. Zschornack, *Handbook of X-Ray Data*, Springer-Verlag Berlin Heidelberg, 2007.

27  L. J. Ament, M. van Veenendaal, T. P. Devereaux, J. P. Hill and J. van den Brink, *Rev. Mod. Phys.*, 2011, **83**, 705.

28  A. Kotani and S. Shin, *Rev. Mod. Phys.*, 2001, **73**, 203.

29  S. Mukamel, D. Healion, Y. Zhang and J. D. Biggs, *Annu. Rev. Phys. Chem.*, 2013, **64**, 101.

30  J. D. Biggs, Y. Zhang, D. Healion and S. Mukamel, *Proc. Natl. Acad. Sci. U. S. A.*, 2013, **110**, 15597.

31  Y. Zhang, J. D. Biggs, N. Govind and S. Mukamel, 2014, submitted.

32  M. Beye, S. Schreck, F. Sorgenfrei, C. Trabant, N. Pontius, C. Schüßler-Langeheine, W. Wurth and A. Fölisch, *Nature*, 2013, **501**, 191.

33  C. Weninger, M. Purvis, D. Ryan, R. A. London, J. D. Bozek, C. Bostedt, A. Graf, G. Brown, J. J. Rocca and N. Rohringer, *Phys. Rev. Lett.*, 2013, **111**, 233902.

34  D. Healion, H. Wang and S. Mukamel, *J. Chem. Phys.*, 2011, **134**, 124101.

35  J. D. Biggs, Y. Zhang, D. Healion and S. Mukamel, *J. Chem. Phys.*, 2012, **136**, 174117.

36  J. D. Biggs, Y. Zhang, D. Healion and S. Mukamel, *J. Chem. Phys.*, 2013, **138**, 144303.

37  P. Kukura, D. W. McCamant and R. A. Mathies, *Annu. Rev. Phys. Chem.*, 2007, **58**, 461.

38  J. M. Rhinehart, J. R. Challa and D. W. McCamant, *J. Phys. Chem. B*, 2012, **116**, 10522.

39  K. E. Dorfman, B. P. Fingerhut and S. Mukamel, *J. Chem. Phys.*, 2013, **139**, 124113.

40  S. Mukamel and J. D. Biggs, *J. Chem. Phys.*, 2011, **134**, 161101.

41  L. S. Cederbaum, W. Domcke, J. Schirmer and W. V. Niessen, in *Adv. Chem. Phys.*, ed. I. Prigogine and S. A. Rice, John Wiley & Sons, Inc., 1986, pp. 115–159.

42  R. Weinkauf, P. Schanen, D. Yang, S. Soukara and E. Schlag, *J. Phys. Chem.*, 1995, **99**, 11255.

43  M. J. Frisch, G. W. Trucks, H. B. Schlegel, G. E. Scuseria, M. A. Robb, J. R. Cheeseman, G. Scalmani, V. Barone, B. Mennucci, G. A. Petersson, H. Nakatsuji, M. Caricato, X. Li, H. P. Hratchian, A. F. Izmaylov, J. Bloino, G. Zheng, J. L. Sonnenberg, M. Hada, M. Ehara, K. Toyota, R. Fukuda, J. Hasegawa, M. Ishida, T. Nakajima, Y. Honda, O. Kitao, H. Nakai, T. Vreven, J. J. A. Montgomery, J. E. Peralta, F. Ogliaro, M. Bearpark, J. J. Heyd, E. Brothers, K. N. Kudin, V. N. Staroverov, R. Kobayashi, J. Normand, K. Raghavachari, A. Rendell, J. C. Burant, S. S. Iyengar, J. Tomasi, M. Cossi, N. Rega, J. M. Millam, M. Klene, J. E. Knox, J. B. Cross, V. Bakken, C. Adamo, J. Jaramillo, R. Gomperts, R. E. Stratmann, O. Yazyev, A. J. Austin, R. Cammi, C. Pomelli, J. W. Ochterski, R. L. Martin, K. Morokuma, V. G. Zakrzewski, G. A. Voth, P. Salvador, J. J. Dannenberg, S. Dapprich, A. D. Daniels, Ö. Farkas, J. B. Foresman, J. V. Ortiz, J. Cioslowski and D. J. Fox, *Gaussian 09, Revision C.01*, Gaussian Inc., Wallingford, CT, 2009.

44  A. D. Becke, *J. Chem. Phys.*, 1993, **98**, 5648.

45  P. J. Stephens, F. J. Devlin, C. F. Chabalowski and M. J. Frisch, *J. Phys. Chem.*, 1994, **98**, 11623.

46  M. Stener, G. Fronzoni and M. de Simone, *Chem. Phys. Lett.*, 2003, **373**, 115.

47  N. A. Besley and A. Noble, *J. Phys. Chem. C*, 2007, **111**, 3333.

48  S. DeBeer-George, T. Petrenko and F. Neese, *Inorg. Chim. Acta*, 2008, **361**, 965.

49  K. Lopata, B. E. Van Kuiken, M. Khalil and N. Govind, *J. Chem. Theory Comput.*, 2012, **8**, 3284.

50  Y. Zhang, J. D. Biggs, D. Healion, N. Govind and S. Mukamel, *J. Chem. Phys.*, 2012, **137**, 194306.

51  T. H. Dunning Jr., *J. Chem. Phys.*, 1989, **90**, 1007.

52  M. Valiev, E. Bylaska, N. Govind, K. Kowalski, T. Straatsma, H. van Dam, D. Wang, J. Nieplocha, E. Apra, T. Windus and W. de Jong, *Comput. Phys. Commun.*, 2010, **181**, 1477.

53  S. Hirata and M. Head-Gordon, *Chem. Phys. Lett.*, 1999, **314**, 291.

54  Y. Zhang, D. Healion, J. D. Biggs and S. Mukamel, *J. Chem. Phys.*, 2013, **138**, 144301.

55  H. Ren, Z. Lai, J. D. Biggs, J. Wang and S. Mukamel, *Phys. Chem. Chem. Phys.*, 2013, **15**, 19457.

56  A. V. Oppenheim and R. W. Schafer, *Discrete Time Signal Processing*, Prentice, Hall Signal Processing, Prentice Hall, New Jersey, USA, 3rd edn, 2009.

57  M. Abramowitz and I. A. Stegun, *et al.*, *Handbook of mathematical functions*, Dover, New York, vol. 1, 1972.

58  J. Olivero and R. Longbothum, *J. Quant. Spectrosc. Radiat. Transfer*, 1977, **17**, 233.